KTH Fysik

In-Beam Spectroscopy of the Extremely Neutron Deficient Nuclei ^{169}Ir and ^{110}Xe

MIKAEL SANDZELIUS

Licentiate Thesis in Physics
Stockholm, Sweden, 2007

TRITA-FYS 2007:41
ISSN 0280-316X
ISRN KTH/FYS/–07:41–SE
ISBN 978-91-7178-692-8

KTH Fysik
SE-100 44 Stockholm
SWEDEN

Akademisk avhandling som med tillstånd av Kungl Tekniska högskolan framläges till offentlig granskning för avläggande av Teknologie Licentiatexamen 14 Juni 2007 kl 15.00 i Sal FB 41, Albanova university centrum, Roslagstullsbacken 21, Stockholm.

Tryck: Universitetssevice US AB

Abstract

This thesis describes new results obtained from experimental studies of the extremely neutron-deficient isotopes ^{169}Ir and ^{110}Xe, close to the proton drip-line. The experiments use state-of-the-art equipment for nuclear spectroscopy where a large high-resolution Germanium-detector array is coupled to a high-transmission recoil separator and using the highly selective recoil-decay tagging technique. The work is based on two experiments performed at the Accelerator Laboratory of the University of Jyväskylä, Finland. The experimental techniques used are described as are the experimental set-ups. Comparison between experimental results and theoretical predictions are made. The thesis also briefly summarises the theoretical models employed to interpret the experimental results.

The results for ^{169}Ir point to a rotational-like behaviour of a moderately deformed nucleus exhibiting triaxial shape. The experimental results do not fully agree with theoretical predictions for the shape evolution of the neutron-deficient iridium isotopes, approaching the proton drip-line. The results for ^{110}Xe indicate an emergence of enhanced collectivity near the N=Z line in the region of the nuclear chart above ^{100}Sn. These findings are interpreted as a possible effect of increased neutron-proton isoscalar pair correlations, a residual interaction effect not accounted for in present-day nuclear models.

List of Publications

This thesis is based on the first two papers in the list.

1. First identification of excited states in ^{169}Ir
   M. Sandzelius, C. Scholey, B. Cederwall, E. Ganioğlu, K. Andgren, D.E. Appelbe, C.J. Barton, T. Bäck, S. Eeckhaudt, T. Grahn, P.T. Greenlees, B. Hadinia, A. Johnson, P.M. Jones, D.T. Joss, R. Julin, S. Juutinen, H. Kettunen, K. Lagergren, M. Leino, A.-P. Leppänen, P. Nieminen, R.D. Page, J. Pakarinen, J. Perkowski, P. Rahkila, J. Simpson, J. Uusitalo, K. Van de Vel, D.D. Warner, D.R. Wiseman, R. Wyss
   Accepted for publication in Phys. Rev. C

2. Identification of Excited States in the $N = Z + 2$ Nucleus ^{110}Xe: Evidence for Enhanced Collectivity Near the $N = Z = 50$ Double Shell Closure
   M. Sandzelius, B. Hadinia, B. Cederwall, K. Andgren, E. Ganioğlu, I.G. Darby, M. Dimmock, S. Eeckhaudt, T. Grahn, P. Greenlees, E. Ideguchi, P.M. Jones, D.T. Joss, R. Julin, S. Juutinen, A. Khaplanov, M. Leino, L. Nelson, M. Nyman, R.D. Page, J. Pakarinen, E.S. Paul, M. Petri, P. Rahkila, J. Sarén, C. Scholey, J. Sorri, J. Uusitalo, R. Wadsworth, R. Wyss
   Submitted to Phys. Rev. Lett.

3. First identification of excited states in ^{106}Te and evidence for isoscalar-enhanced vibrational collectivity
   B. Hadinia, B. Cederwall, J. Blomqvist, E. Ganioğlu, P.T. Greenlees, K. Andgren, I.G. Darby S. Eeckhaudt, E. Ideguchi, P.M. Jones, D.T. Joss, R. Julin, S. Juutinen, S. Ketelhut, K. Lagergren, A.-P. Leppänen, M. Leino, M. Nyman, J. Pakarinen, E.S. Paul, M. Petri, P. Rahkila, **M. Sandzelius**, J. Sarén, C. Scholey, J. Uusitalo, R. Wadsworth, R. Wyss
   Phys. Rev. C**72**, 041303 (2005)

4. In-beam and decay spectroscopy of very neutron deficient iridium nuclei
   C. Scholey, **M. Sandzelius**, S. Eeckhaudt, T. Grahn, P.T. Greenlees, P.M. Jones, R. Julin, S. Juutinen, M. Leino, A.-P. Leppänen, P. Nieminen, M. Nyman, J. Perkowski, J. Pakarinen, P. Rahkila, J. Uusitalo, K. Van de Vel, B. Cederwall, B. Hadinia, K. Lagergren, D.T. Joss, D.E. Appelbe, C.J. Barton,

J. Simpson, D.D. Warner, I.G. Darby, R.D. Page, E.S. Paul, D. Wiseman
J. Phys. G 31 (10) 1719 (2005)

5. Isomer spectroscopy in ^{254}No
R.-D. Herzberg, P.T. Greenlees, P.A. Butler, G.D. Jones, I.G. Darby, S. Eeckhaudt, T. Grahn, C. Gray-Jones, F.P. Hessberger, P.M. Jones, R. Julin, S. Juutinen, S. Ketelhut, M. Leino, A.-P. Leppänen, S. Moon, M. Nyman, R.D. Page, J. Pakarinen, A. Pritchard, P. Rahkila, **M. Sandzelius**, J. Sarén, C. Scholey, A. Steer, J. Uusitalo, M. Venhart
Phys. Scr. 2006 No T125 (July 2006) 73-77

6. Collectivity and Configuration Mixing in ^{186,188}Pb and ^{194}Po
T. Grahn, A. Dewald, O. Möller, R. Julin, C.W. Beausang, S. Christen, I.G. Darby, S. Eeckhaudt, P.T. Greenlees, A. Görgen, K. Helariutta, J. Jolie, P.M. Jones, S. Juutinen, H. Kettunen, T. Kröll, R. Krücken, Y. Le Coz, M. Leino, A.-P. Leppänen, P. Maierbeck, D.A. Meyer, B. Melon, P. Nieminen, M. Nyman, R.D. Page, J. Pakarinen, P. Petkov, P. Rahkila, B. Saha, **M. Sandzelius**, J. Sarén, C. Scholey, J. Uusitalo
Phys. Rev. Lett. **97**, 062501 (2006)

Contents

Chapter 1

Introduction

This thesis is based on the study of the extremely neutron deficient atomic nuclei ^{169}Ir and ^{110}Xe (**papers I** and **II** in the List of Publications). The experimental approach in order to unravel the intrinsic structure of these nuclei is described, and the results are compared with theoretical models.

The nucleus can be regarded as being made of neutrons and protons interacting via the strong force. However, the forces between the nucleons in a nucleus are not due to the bare interactions between the constituent quarks, but rather effective forces that can be schematically described, e.g with meson exchange. Not only are the low-energy properties of the strong interaction poorly known, the effective forces acting inside a nucleus are even more so. Depending on the relative abundance of protons and neutrons different properties, e.g deformations, are expected. It is believed that nuclear deformation has a strong dependence on the residual proton-neutron interaction. Therefore, nuclei far from stability behave differently than stable isotopes. It is expected that models describing features of stable nuclei may not easily be extrapolated to nuclei far from stability. This gives the impetus to study these "exotic" nuclei in order to test the validity of nuclear models describing the stable and moderately unstable nuclei and provide vital additions, or constraints, for these models.

The atomic nucleus is a particularly complex many-body system not fully understood. No single theoretical model can, to date, fully describe every nucleus in the Segré chart (map of all stable and unstable nuclei), and predict their excitation modes. The excitation modes of the nucleus can be of collective or single-particle nature. A collective excitation is characterised by many nucleons participating in the motion in a coherent manner. Rotation of the whole nucleus is an example of this. Single particle excitations promote individual protons or neutrons to higher lying orbitals. All excitation modes normally mostly deexcite by γ-ray emission. By detecting these γ rays and ordering them in a cascade, where the transitions are in mutual coincidence with each other, it is possible to construct a level scheme. Through this, it is possible to extract information on the structural properties like

the deformation of the nucleus. Different types of excitation modes leave different signatures in the level scheme. Therefore, interpreting the structure of the level scheme gives vital clues to the behaviour and the shape of the nucleus.

The shell model has been the most successful model for describing the nuclei in the vicinity of magic numbers. In the shell model the neutrons and protons are described to move independently of each other inside a mean-field potential made up from the main interactions with all the other nucleons. Any interaction not included in the mean-field is known as a residual interaction, e.g. the nucleon-nucleon pairing interaction. A detailed neutron-proton interaction is not explicitly accounted for in the shell model. Since protons and neutrons are fermions they obey the Pauli principle stating that two identical fermions cannot occupy the same quantal state. As a consequence the protons as well as the neutrons, normally move in different orbits in the nucleus. However, in N≈Z nuclei neutron and proton orbitals can have large spatial overlaps resulting in a strong residual neutron-proton interaction leading to great deviations from shell model predictions. This possible effect plays an important role in the interpretation of the ^{110}Xe data. In the N=Z+2 ^{110}Xe nucleus the few valence nucleons outside a closed shell occupy identical orbitals, and neutrons and protons may therefore be susceptible to dynamical coupling.

Certain nuclei may adopt triaxial shapes and can be excited through rotation around a non-symmetric axis. This is the case in ^{169}Ir where the rotational-like spectrum indicates a triaxially deformed nucleus, meaning that all axes have different lengths. However, it shall be noted that a clear and unique experimental signature of triaxiality is not available. The odd-mass nuclei in the mass A∼170 region also offer a possibility to study the interplay between collective and single particle motion. The odd single particle can be interpreted as coupled to the deformed even-even core built of all the other nucleons and hence serve as a probe of the nuclear shape. Depending on the nuclear deformation different single particle configurations are favoured and the relative energies between these also contain information on the nuclear shape. In the vicinity of closed nucleon shells one expects single-particle excitations to dominate over collective phenomena. The nucleus ^{169}Ir lies in the mass region between the neutron mid-shell and the closed shell at $N = 82$. In this transitional region, ^{169}Ir offers the opportunity to study the emergence of collective behaviour, such as rotations, from a single particle regime. It is therefore a rich hunting ground for numerous nuclear structure phenomena. In some cases there can be different states in the nuclues with virtually the same excitation energy but with quite different structures. This phenomenon is know as shape coexistence. Although not evident in the nucleus under study in this work there are several examples in this area of the nuclear landscape where this phenomenon is manifested.

The results for ^{110}Xe and ^{169}Ir are presented here for the first time.

Chapter 2

Experimental Techniques

The fusion-evaporation experiments producing the two nuclei ^{169}Ir and ^{110}Xe studied in this work were performed at the JYFL Accelerator Laboratory at the University of Jyväskylä in Finland. The K130 cyclotron facility was used to accelerate the ^{60}Ni and ^{58}Ni ions and deliver them on to the ^{112}Sn and ^{54}Fe targets, respectively. Results were obtained with the JUROGAM Ge-detector array. The experimental techniques used to study these exotic nuclei will be described in two steps. First there will be a description of the dynamics and physical mechanisms involved in order to produce the nuclei in question, and secondly, the actual experimental set-up and the techniques used to detect and study these nuclei will be outlined.

2.1 Production of the Nuclei

Producing and detecting nuclei far from stability offer significant experimental challenges. They are very short-lived, often in the micro- to millisecond region, before they decay via charged particle emission (α, β or proton decay). They also come with small production cross-sections, usually in the mb-μb region, but sometimes even as small as a few tens of nb (which is around the current limit for in-beam spectroscopy) and below. Stable isotopes have enough neutrons to counterbalance the Coulomb repulsion from all the protons, thereby holding the nucleus together. With neutron deficient nuclei there is a relative excess of protons compared to the number of neutrons for it to be stable against charged particle emission. The further from the line of stability (a specific ratio of protons/neutrons) on the neutron-deficient side of the stability line, the shorter the half-life gets and the more unstable the nucleus is to alpha particle emission. Beyond the proton drip-line, where the the proton separation energy $S_p < 0$, the nucleus is also unstable against proton emission.

Since these nuclei are unstable and hence do not occur naturally they have to be produced artificially in the laboratory. This is achieved via fusion-evaporation reactions which is the most efficient method to produce neutron-deficient nuclei.

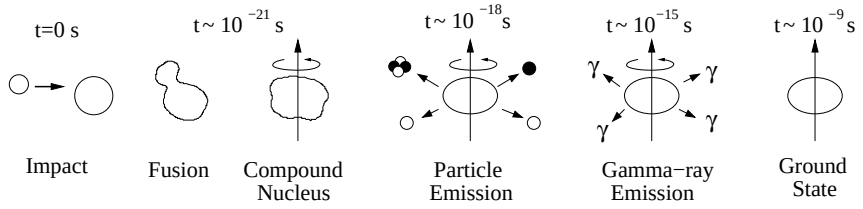

Figure 2.1: Schematic view of the production process of nuclei with subsequent fusion-evaporation of particles and γ-ray deexcitation down to the ground state. The picture is adopted from [1].

Both ^{169}Ir and ^{110}Xe were produced by an incindent beam of accelerated ions impinging upon a stable target. If the kinetic energy of the incoming ions (beam energy) is sufficient to overcome the Coulomb barrier, and if one of them manages to strike a target nucleus, the two nuclei may merge via a fusion reaction into a highly excited compound nucleus. The compound nucleus is created at a very high spin and excitation energy and will therefore quickly 'boil off' (evaporate) particles, such as alpha particles, protons and neutrons. In order to cool down further, emission of γ rays follows down to a region close to the yrast line. These statistical γ rays carry away energy from the compound nucleus but are not so efficient in removing spin. The nucleus further deexcites with γ-ray transitions along (or close to) the yrast line (states with lowest excitation energy for a given spin) down to either the ground state or an isomeric state. Figure 2.1 schematically illustrates the production process with the different phases and emission times involved. If the target is thin enough ($\sim$1-5 μm) the recoiling final nucleus will not be stopped in the target but continues to travel through the target material. Typically, deexcitation of the nucleus takes place within the target or just a few cm downstream from it in the beam direction.

2.2 Gamma-Ray Detection

Detection of the γ rays emitted in the reactions was made using an array of germanium detectors. They have a superior energy resolution (FWHM $\sim 2-3$ keV at E_γ=1 MeV) compared with other detector materials. Good energy resolution is of great importance since many γ rays might have similar energies. The solid state germanium detectors used in both experiments were arranged into a large detector array surrounding the target position with a large fraction of the full solid angle. This enables detection of high multiplicity events in which several γ-ray transitions form a cascade of mutual coincident transitions.

A γ-ray spectrum is a one dimensional histogram of γ-ray energies. Besides containing the photo peak γ-ray energies the γ-ray spectrum has two additional

components: a background "continuum" formed by the high energy statistical photons and γ rays that have partially escaped from the germanium detector. The latter is known as Compton scattering and occurs when a γ-ray scatters out of the detector, not depositing its full energy. However, this Compton continuum can be greatly reduced through *Compton suppression*. Surrounding each germanium detector is a shield of BGO (Bismuth Germinate) detectors. BGO is a dense material with good scintillation properties giving excellent photon detection efficiency. When a photon scatters out from a germanium detector and interacts in the surrounding BGO-shield the BGO signal will appear in coincidence with the signal from the germanium detector thereby making it possible to veto the photon from being stored by the data acquisition system.

2.2.1 Doppler Correction

The fusion-evaporation residue continue to travel through the target material and recoil out of the target in the beam direction. The recoiling nucleus moves at a speed almost in the relativistic regime, typical values are $\sim 3-5\%$ of the speed of light. Therefore, the γ rays will be *Doppler shifted* depending on at what angle they are emitted relative to the beam direction. Detectors placed at an angle larger than 90° relative the beam direction will register a lower γ-ray energy and detectors situated at a angle less than 90° from the beam direction will record a higher γ-ray energy than the emitted one. This Doppler shift has to be accounted and compensated for through the relation:

$$E'_\gamma = E_\gamma \frac{\sqrt{1-\beta^2}}{1-\beta\cos\theta} \approx E_\gamma(1+\beta\cos\theta) \quad \text{for } \beta << 1 \tag{2.1}$$

E'_γ denotes the γ-ray energy recorded by the detector and E_γ is the unshifted γ-ray energy emitted from a nucleus at rest. The detector angle relative to the beam direction is θ and the velocity of the recoiling nucleus is taken into account in the factor $\beta = v/c$. The data acquisition system stores information at what angle relative to the beam direction a γ-ray has been detected so that a proper Doppler shift compensation can be performed in the off-line analysis.

2.2.2 Doppler Broadening

Depending on the width of the germanium crystal the detector will cover a certain finite opening angle with respect to the recoil-velocity direction and the target position. The detector opening angle has to be kept small enough in order to keep the *Doppler broadening* at a minimum. But at the same time the germanium crystal has to be large enough in order to minimise the number of γ rays that Compton scatter out of the detector. The Doppler broadening ΔE_γ is given by differentiating equation 2.1 with respect to θ, leading to the relation:

$$\Delta E_\gamma \approx E'_\gamma \frac{v}{c} \sin\theta \, \Delta\theta \tag{2.2}$$

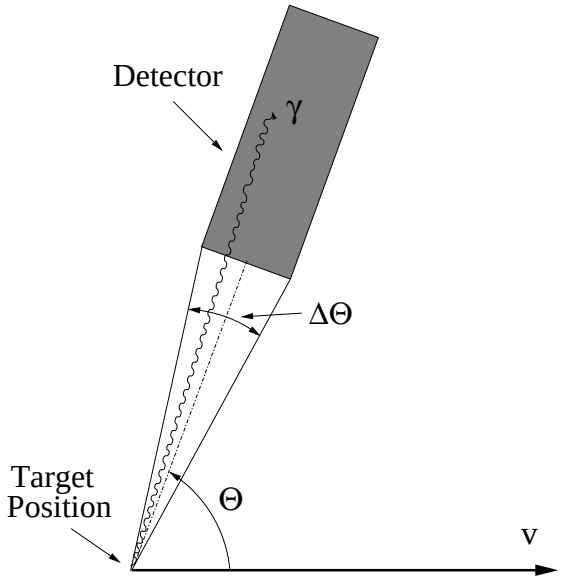

Figure 2.2: The opening solid angle ($\Delta\theta$) of the detector causes the γ-ray peak to be Doppler broadened. The Doppler broadening also depends on the relative angle (θ) of the detector from the recoil-velocity direction

where E'_γ is the measured γ-ray energy and θ is the detector angle relative to the recoil-velocity direction. The Doppler broadening increases with increasing γ-ray energy and is more pronounced at an angle of 90° from the recoil-velocity direction. The angular parameters responsible for the Doppler broadening are shown in figure 2.2.

Peaks always appear broader for larger γ-ray energies in the spectrum and can be more difficult to resolve than lower down in the spectrum. Given a typical $v/c = 0.03$, a detector diameter of 5 cm situated at 20 cm from the target, and measuring a 500 keV γ-ray in the 90° direction yields a Doppler-broadening of ~ 4 keV. Hence, the Doppler broadening typically dominates over the intrinsic energy resolution and it is crucial that the detector array has a good angular granularity in order to minimize this effect.

2.2.3 Coincidence Measurements

A high detector granularity is also needed in order to avoid multiple hits on a single detector by more than one γ-ray from a cascade of emitted γ rays. The number of detected γ rays in a single cascade is called *fold* and the total number of γ rays in a cascade is called *multiplicity*. In these in-beam decay measurements the

fold is typically around 1-6. If two γ rays strike the same detector simultaneously these events will fall outside the full photo peak, instead they will contribute to the background continuum. If two γ rays are detected in different detectors at approximately the same time they are said to be *in coincidence* with one another, and are therefore interpreted as belonging to the same cascade from one deexciting nucleus created in the reaction. In these experiments the coincidence time condition between two γ rays in a cascade is set to be 100 ns.

2.3 The JUROGAM Detector Array

Gamma-ray detection is performed with the JUROGAM detector array. It consists of 43 EUROGAM [2] phase I and GASP [3] type Compton-suppressed high-purity germanium detectors. The detector array covers almost 2/3 of the total solid angle around the target position. The detectors are arranged in six different rings at different angles relative to the beam direction, with five detectors at 158°, ten at 134°, ten at 108°, five at 94°, five at 86° and eight at 72°. In this configuration JUROGAM has a total photo-peak efficiency of 4.2% at 1.3 MeV. The JUROGAM detector array is depicted in figure 2.3.

2.4 Recoil Separation

After the nuclei have been produced they will travel downstream from the target, along with the ions of the primary beam that did not react with target nuclei, into the gas-filled magnetic separator, RITU. In RITU (Recoil Ion Transport Unit) a beam-recoil separation is obtained through deflection of moving charged particles by a strong dipole magnetic field. In this way good recoils (fusion evaporation residues) can be isolated from primary beam components.

2.4.1 The RITU Gas-Filled Recoil Separator

The RITU gas-filled recoil separator [4, 5] operates in a QDQQ magnetic configuration (see figure 2.4). Compared to a vacuum separator, a gas-filled separator, such as RITU, has a significantly higher transmission efficiency but a lower mass resolution. RITU can have transmission efficiencies of $\sim$50% for favourable reactions, while a vacuum separator usually has $<$10% transmission efficiency. RITU has, in addition to the two focusing quadrupole magnets (Q) downstream from the dipole magnet (D), a strongly vertical-focusing quadrupole magnet in front of the dipole magnet. This enables a higher angular acceptance ($\sim$10 msr) of recoiling ion residues and an increase in transmission efficiency. In a vacuum separator only two or three charge states can be collected and transmitted through the separator, leading to low transmission efficiency, but higher selectivity.

The recoiling ions emerging from the target after the fusion reaction have a wide distribution of charge states. Multiple scattering of the recoiling ions on

Figure 2.3: A close-up picture of the JUROGAM germanium detector array. The ion beam enters into the array from the beam line shown by the arrow at the bottom of the picture. The picture is taken from reference [9].

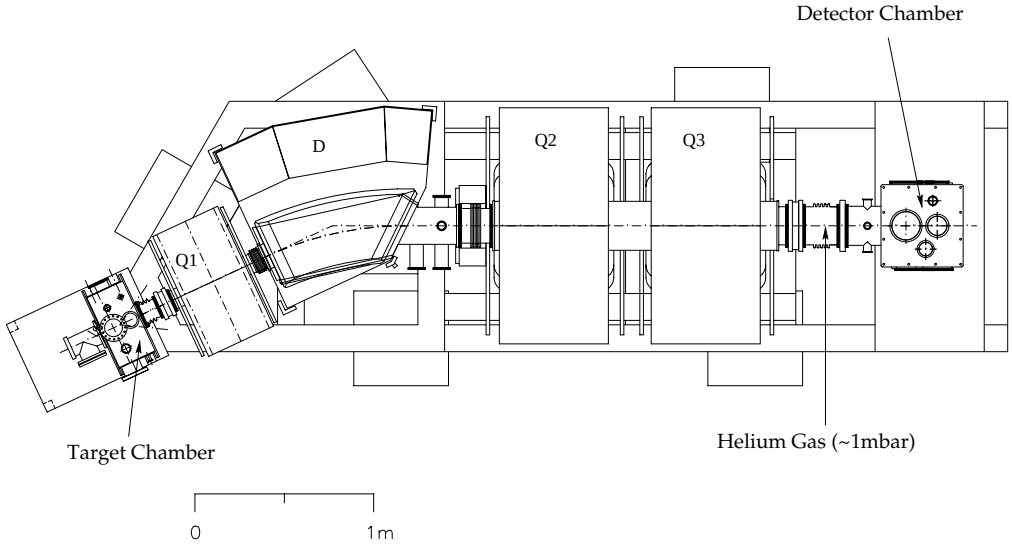

Figure 2.4: Schematic overview of the RITU recoil separator. The focusing quadrupole magnets are indicated with a Q, and D is the bending dipole magnet. The figure is taken from reference [9].

the gas molecules induces a velocity-dependent charge equilibration that serves to separate the much faster beam particles from the fusion-evaporation residues. The gas has to be dense enough to provide a small mean free path between charge changing collisions compared to the flight distance through the separator. Figure 2.5 demonstrates the difference in separation techniques between a vacuum separator and a gas-filled one. The acceptance of nearly all charge states gives the significant higher transmission efficiency than in a vacuum separator. The magnetic field region of the separator is filled with a constant flow of helium gas. The key is to keep the pressure of the gas on a certain level to enable the optimum charge state focusing in order to minimise the image hit pattern at the focal plane. Typical values for the helium gas pressure is ~ 1 mbar.

The magnetic rigidity is the important factor of the dipole magnet ion deflection capacity. It can be described (to first order) by the formula [6]

$$B\rho = \frac{mv}{q_{ave}} = \frac{mv}{[(v/v_0)eZ^{1/3}]} = 0.0227\frac{A}{Z^{1/3}} \quad [\mathrm{Tm}] \tag{2.3}$$

where B is the magnetic field strength, ρ the bending radius of the ions, A, Z, v and m are the mass number, proton number, velocity and the rest mass of the recoiling ion, respectively. The expression for $q_{ave} = (v/v_0)eZ^{1/3}$ is obtained from

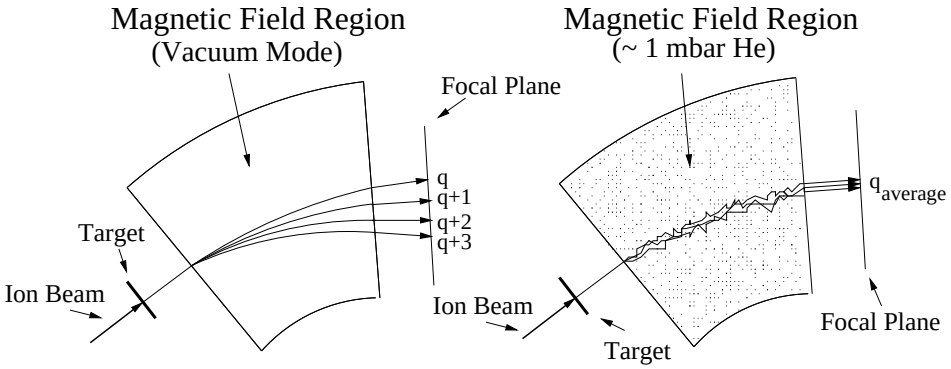

Figure 2.5: Schematic illustration of the effect of average charge collection of the recoils in a gas-filled separator. The magnetic field points perpendicular out from the page.

the Thomas-Fermi model [7] of the atom where v_0 is the Bohr velocity = $c/137$ m/s. The average charge state is proportional to the velocity of the ions, thus charge and velocity focusing is achieved by the gas-filled separator. It can be seen from equation 2.3 that separation of the primary beam from the recoiling ions is usually excellent in asymmetric reactions (where target- and beam ion mass number are very different) since the $A/Z^{1/3}$ factor will assure different bending trajectories. The trajectory of the primary beam is usually sufficiently different from that of the recoiling nuclei to give a suppression in the order of $10^{-12}-10^{-15}$. However, in near symmetric reactions, as in the case of producing ^{110}Xe (^{54}Fe+^{58}Ni $\longrightarrow$^{110}Xe+2n), beam suppression can be difficult since the rigidity of the primary beam is close to that of the fusion-evaporation residues, leading to a reduced beam suppression factor. For these types of symmetric reactions RITU is equipped with an mobile adjustable beam stopper. It is a tantalum strip inserted just downstream of the dipole chamber beam dump in order to physically stop primary beam and scattered beam components. In practice, although this procedure reduces primary beam ions from being transported to the focal plane, beam suppression factors as in more asymmetric reactions are seldom achieved.

After recoil separation two quadrapole magnets focus the recoiling nuclei so they can be implanted at the focal plane of RITU.

2.5 The GREAT Spectrometer

The GREAT (Gamma Recoil Electron Alpha Tagging) [8] spectrometer is situated at the focal plane of RITU (see figure 2.7). It is a composite detector system consisting of two double-sided silicon strip detectors (DSSD), a multi-wire proportional

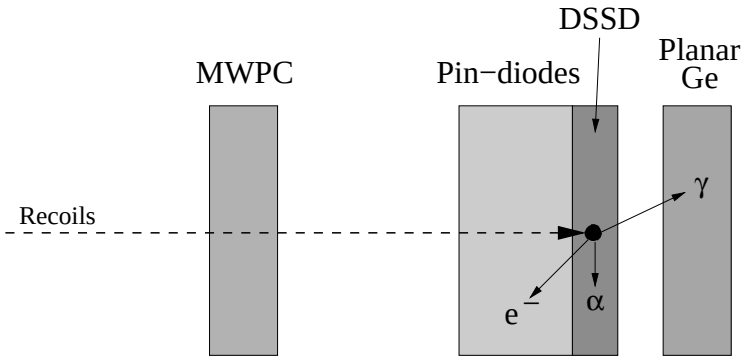

Figure 2.6: A schematic side view of the GREAT detectors. Recoils are implanted in the DSSD where subsequent charge particle (α particle and proton) emission is detected. The PIN-diodes can be used for detecting electrons and escaped α particles. The planar Ge-detector and the segmented clover detectors (not pictured here) are used for detection of delayed (isomeric) γ-ray transitions.

gas-counter (MWPC), a planar germanium detector and an array of 28 Si PIN diode detectors (see figure 2.6). In addition, a high-efficiency segemented Clover-type germanium detector is situated directly above the GREAT detector in order to detect high energy γ rays.

The recoils are implanted in the DSSD. The DSSD consists of two active windows measuring 60×40 mm^2 with 200 individual strips at a 1 mm pitch in both directions leading to 4800 independent pixels. The active area of the DSSD normally covers about 85% of the focal-plane distribution of fusion products. The DSSD is used to detect the incoming recoils and their subsequent charge particle decay (protons or alpha particles). The high granularity of the detector enables long correlation search times between an implanted recoil and its charged particle decay when the implatation rate is low, or vice versa, high implantation rates can be allowed if the experiment favours short correlation times between recoil implantation and a charged particle decay.

2.6 The Total Data Readout System

The data acquisition system used for the JUROGAM+RITU+GREAT set-up is a triggerless system. Conventional methods of data collection for recoil-gating type of experiments have previously been made with the use of a common hardware trigger. The trigger then opens up a time window during which data from an event is registred. This causes dead time losses, since additional data coming within this time window cannot be processed before the event is read out. These “common” dead time losses can easily reach tens of percent in typical experiments. A way

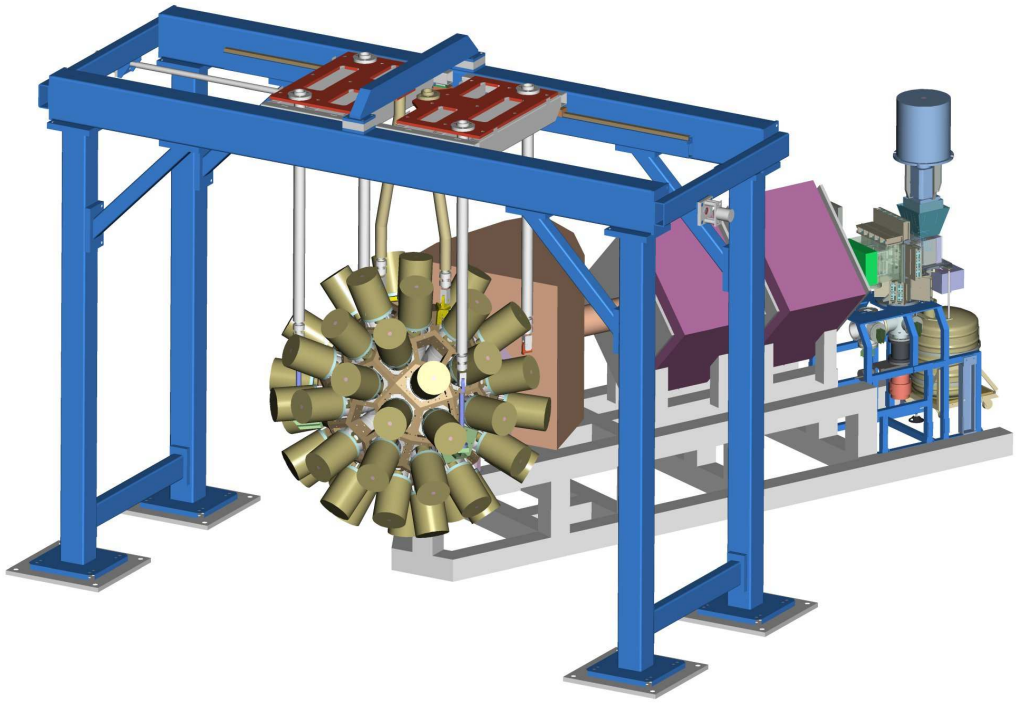

Figure 2.7: A schematic drawing of the experimental set-up. The JUROGAM Ge-array is shown in the foreground followed by the RITU recoil separator and the GREAT spectrometer situated at the RITU focal plane. The figure is taken from reference [9].

around the trouble with common dead time losses is to avoid a trigger altogether. In the Total Data Readout (TDR) system [10], all channels are running independently and each registered signal is associated with a 100 MHz clock signal. The systems 'time resolution' is thus in effect 10 ns. The only dead time arising is from the analog shaping and conversion time from each individual channel, which is in the order of $\sim$10 μs. Since the firing rate of an individual detector is much less than the trigger rate of the entire detector system this gives much smaller dead time losses. The difference in dead time losses can be quantified through the so called Nonparalyzable model [11] of the dead time. In this model a fixed dead time is assumed to follow each true event, and events which occur during that dead time period are assumed to be lost. Let n be the true event rate, m the recorded count rate and τ the system dead time. The fraction of all time that the detector system

is dead is then given by the product $m\tau$, and the rate at which true events are lost is then $nm\tau$. This loss rate can also be expressed as $n - m$ and therefore

$$n - m = nm\tau \tag{2.4}$$

Solving for the detected interaction rate, m, yields

$$m = \frac{n}{1 + n\tau} \tag{2.5}$$

For low count rates ($n << 1/\tau$) equation 2.5 can be approximated with

$$m \approx n(1 - n\tau) \tag{2.6}$$

For a conventional data acqusition system used for this type of experiments the event trigger would normally be determined by the DSSD. With a trigger rate of $n = 4000$ Hz and a common dead time of $\tau \approx 30$ μs equation 2.6 gives a true detection fraction of $m/n = 0.88$ and hence a dead time loss of 12%. For a triggerless system the average individual detector count rate could be ∼0.5 kHz and the ADC conversion $\tau \approx 10$ μs, yielding an average data loss due to dead time in the order of 1%. Although a direct comparison is not strictly valid, the calculated dead time figures do give an indication of the qualitative difference between the two trigger systems.

The data are merged into a single stream of time stamped data which is then filtered through the Event Builder processor of the data acquisition system for subsequent storage on disc.

The TDR system allows a versatile treatment of the data stream. With 512 channels available in total, the JUROGAM+RITU+GREAT detection system generates vast quantities of data. In order to reduce the storage space of the data and facilitate the data processing, the JUROGAM data are filtered in the Event Builder by using a software trigger to define the event time. In the type of measurements described in this thesis the data acquisition system employs an OR gate in the GREAT spectrometer as a software trigger. It requires a signal in *any* of the GREAT detectors to be recorded for an "event" to start, and JUROGAM data are only stored if they arrive within a preset time window relative to any GREAT signal. This pre-filter software trigger is useful in order to minimise the amount of JUROGAM background data.

The TDR system allows for a flexible handling of the data off-line. The user has a variety of reconstruction possibilities available depending which temporal and spatial correlations in the data that are of interest.

Chapter 3

Data Analysis

The amount of data generated from a single experiment is huge. From a typical seven day experiment several hundreds of gigabytes of data are produced. Although on-line analysis of the data is made continuously during the experiment a full detailed spectroscopic study of all the recorded data is seldom made. Therefore the data have to be stored on disc for off-line analysis.

3.1 The Recoil Decay Tagging Technique

The type of heavy-ion reactions described in this thesis generate a large number of γ rays around the target position. Many γ rays are produced from fission events, deexcitations following Coulomb excitation, transfer reactions and the multitude of open fusion evaporation channels. Most of these are not of primary interest and only serve to obscure the γ rays associated with the nucleus under study. For fusion-evaporation reactions leading to neutron deficient nuclei, often up to a dozen (or more) reaction channels are open, many of which are usually significantly stronger, i.e. have a larger cross section, than the evaporation channel of interest. Therefore, the ability to cleanly select a specific reaction channel is of the utmost importance in order to isolate and assign γ rays to the correct nucleus.

The Recoil-Decay Tagging (RDT) technique offers such a possibility. The RDT technique was first employed in the late eighties at GSI, Darmstadt [12] and further developed at Daresbury Laboratory, U.K. [13]. It is at the same time a powerful and elegant technique to 'weed out' those channels that otherwise would be buried in the "background" from more prolific reaction products. The RDT technique relies on the possibility to identify a specific fusion-evaporation residue by means of its radioactive decay. Heavy nuclei close to the proton drip-line most often decay by alpha or proton emission. Since these particle emissions have discrete and unique energies they offer a signature, or 'tag', on the mother nuclei from which the particles were emitted. If the half life for charged particle emission is not too short compared to the flight time through RITU ($\sim$0.5-1 μs) the radioactive decay

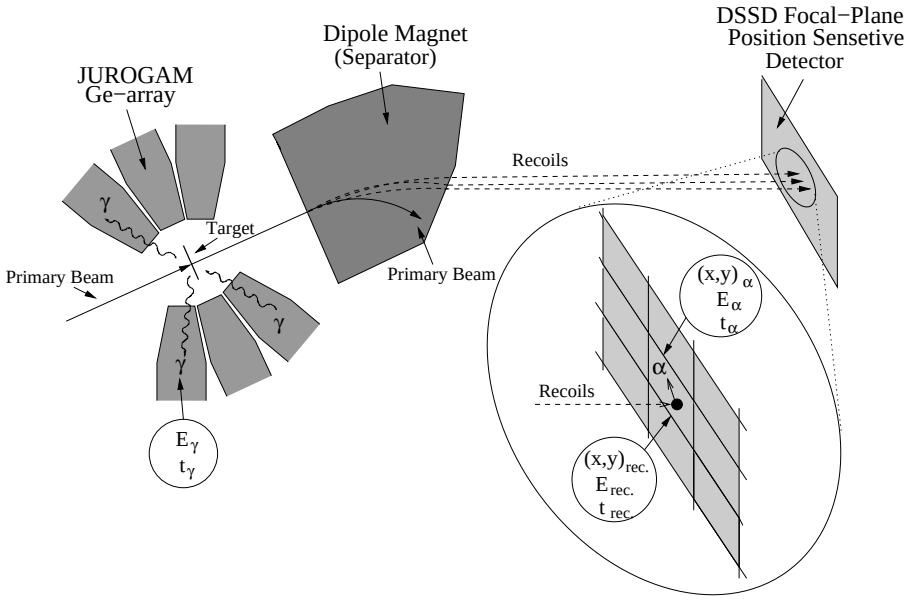

Figure 3.1: Schematic view of the RDT technique. An α decay is detected in the DSSD. Information of the position, energy and time is registered so the mother recoil can be searched for, and tagged, in the same pixel at an earlier time. Correlating back in time allows prompt γ rays at the target position to be associated with the recoil implantation. The perspective of the DSSD is skewed in order to visualise the recoil implantation in a DSSD pixel.

of the fusion product can be detected in the focal plane DSSD, and with proper spatial and temporal correlation with the implanted recoil, prompt γ rays emitted at the target position can be associated with the nucleus that emitted the particle. Figure 3.1 depicts the principles behind the RDT technique. The identification of the implanted recoil is made with its decay particle (α particle or proton). The search time between recoil implantation and the subsequent radioactive decay in the same pixel in the DSSD is usually taken to be three half-lives of the decay in question. Provided the characteristic decay properties (decay energy and half-life) for the nuclei under study are previously known an isotope identification can be made. Sometimes recoil identification is possible even if the decay properties it not previously known.

Just how selective and powerful the RDT technique can be is illustrated in figure 3.2. The top γ-ray spectrum is selected with the condition that a fusion-evaporation residue was detected in delayed coincidence at the RITU focal plane. This spectrum shows γ rays from every fusion-evaporation channel open in the

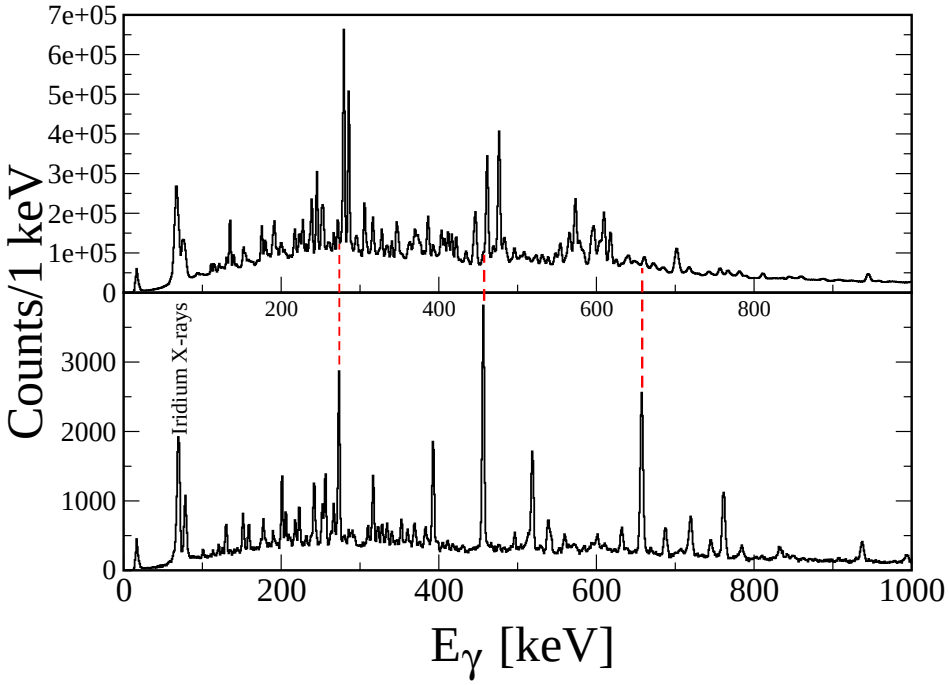

Figure 3.2: Gamma-ray spectra showing prompt γ rays at the target position. The spectrum in the top panel is recoil-gated only, showing the γ rays detected in the experiment from all fusion-evaporation nuclei giving a signal in the DSSD. The spectrum in the bottom panel is recoil-decay tagged with the decay properties of ^{169}Ir. The three strongest transitions are indicated, which cannot be resolved in the total recoil-gated spectrum.

experiment. The bottom panel show prompt γ rays recoil-decay tagged with the characteristic α decay of ^{169}Ir. Without the tagging identification the γ rays belonging to this specific reaction channel would have been out of reach and masked by the stronger channels. It is truly like finding the needle in the hay-stack.

3.2 Recoil Identification

In order to employ the RDT technique properly, a clean recoil identification of the fusion-evaporation residue first has to be made. Although most of the primary beam can be suppressed in the recoil gas-filled separator some beam and scattered beam components are transported to the focal plane and implanted into the DSSD. In order to correlate prompt γ rays with the proper recoil residue the recoils have

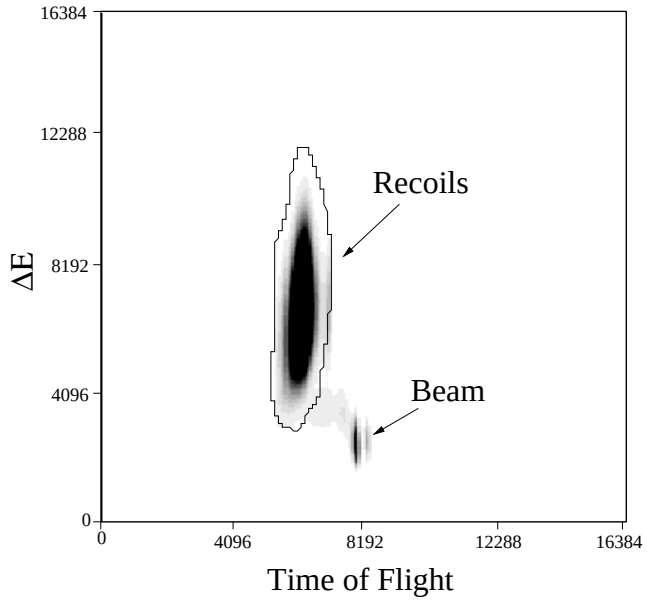

Figure 3.3: Recoil selection in the MWPC. The plot shows energy deposited (ΔE) versus time of flight between the MWPC and the DSSD. The recoils are situated inside the gate used to select them, and beam like particles are well separated to the lower right of the two dimensional gate. Time of flight is increasing from right to left and the axis units correspond to the raw channel number.

to be discriminated from the primary beam and scattered beam components. No direct discrimination is possible but an active discrimination has to be performed in the off-line analysis. The MWPC offers such an opportunity to distinguish reaction products from primary beam and scattered beam components by means of the measured energy loss in the gas-counter and the time of flight as measured by the time difference between the signals from the gas-counter and the DSSD. Energy losses are different for recoils and scattered beam components, and the latter have faster time of flight than the former through the MWPC (see figure 3.3). The energy loss and timing signals can thus be used in conjunction with the DSSD to discriminate scattered beam from good recoils.

There is also the possibility to discard events in the DSSD which are outside an energy range of interest. Primary beam and scattered beam components have greater implantation energy than that of the recoils (see figure 3.4). Once identified, the unwanted high energy events recorded in the strip detector can be vetoed by applying an energy gate. The MWPC can also be used to distinguish recoils passing through it from their subsequent decays. Both events are recorded in the DSSD but

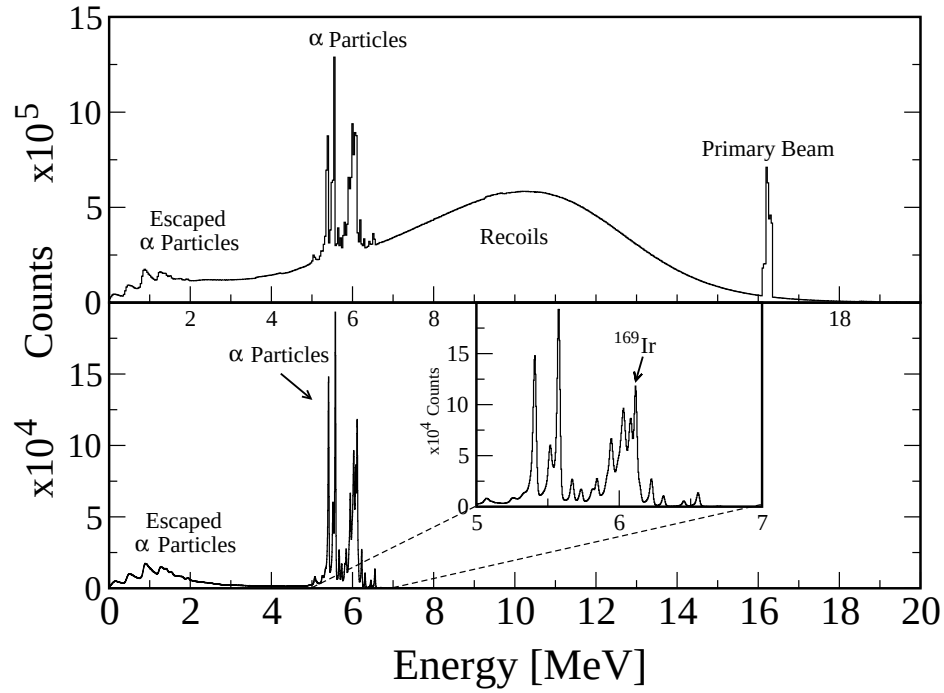

Figure 3.4: Top panel shows the total raw singles spectrum from the GREAT strip detector following the reaction leading to ^{169}Ir. The spectrum shows all events recorded in the DSSD during the experiment. The bottom panel shows events recorded in the DSSD, requiring that the MWPC detector has not fired (i.e. it acts as a veto detector). Only α decay activity is recorded, with the α energy of ^{169}Ir [6117(3) keV] marked in the inset.

only the recoil will deposit a signal in the MWPC, hence a veto from the MWPC will ensure identification of a charged particle decay in the position sensitive DSSD (see figure 3.4).

3.3 Calibration

Before undertaking any analysis of the data, a calibration has to be performed of the different detectors involved in the experiment. Before and after the experiments data is taken through calibration runs. Radioactive sources are placed at the target position and at the focal plane (^{152}Eu, ^{133}Ba and ^{60}Co) and the emitted γ rays are detected. Since the γ-ray energies from the sources are known, the position of the peaks in the resulting spectrum can then be used to make an energy calibration of

each detector. Also, from the relative intensities of the γ rays detected from the sources an efficiency calibration can be made for the JUROGAM Ge-detectors.

Two different functions for fitting the measured peak positions are utilised in these experiments. The data from some detectors usually have very linear dependence of the peak position in the histogram as a function of energy, while others can have quite non-linear behaviour[1]. For the ^{169}Ir analysis a second order polynomial is used to fit the Ge-detector data, while in the case for ^{110}Xe a more elaborate function is utilised to handle the non-linearities. If there are enough data points at the low end of the spectrum, where the non-linear behaviour is most pronounced, there need not to be any problem with the fitting. However, troubles can arise for data which fall outside the range of the calibration sources, especially in the low energy end of the spectrum.

3.4 Sorting Gamma-ray Spectra

The recorded information from the experiments is a reduced time-stamped data stream from the TDR system stored on disc. Events are created by a sorting process using the spatial and temporal correlations that are relevant, e.g. a prompt JUROGAM signal should arrive Δt=flight time before the recoil signal from the DSSD. However, from individual events it is difficult to draw any conclusions of the nucleus of interest. The data has to be *sorted* into spectra. The data is sorted with the Grain software package [14]. Two types of spectra are considered here. There are the singles one-dimensional spectra that show γ-ray intensity as a function of energy. There are also matrices for which coincidences between at least two γ rays is required in order to increment the two-dimensional histogram (the "matrix element"). The higher the fold the more matrix elements are incremented since all combinations of γ rays forming the cascade have to be accounted for, e.g. a fold of three generates increments of six matrix elements in a symmetric γ-γ-correlation matrix. Tagged singles spectra are useful to identify and assign γ rays to a specific nucleus, while a symmetric γ-γ matrix is used to construct a level scheme.

3.5 Producing a Level Scheme

Not much can be said of the nuclear structure from individual γ rays in a singles spectrum. Therefore the γ-ray energy and coincidence information have to be transformed into a level scheme. A level scheme is an ordered decay scheme of excited states constructed from γ rays in mutual coincidence deexciting the nucleus. A γ-ray feeding into an excited level is matched by another one feeding out (deexciting) from the same level. The intensity flow to a state should in principle equal that out from the state. The exception being the ground state or any isomeric state which may decay outside the sensitive time range or by charged particle emission

[1]Most ADC's are quite non-linear for low channel numbers. It is a peculiarity of the TDR timestamping ADC's used at JYFL and quite uncommon in high-resolution spectroscopy set-ups.

outside the scope of the prompt γ-ray regime. There can be several decay paths to or from the same level. Two γ rays feeding or deexciting the same level will not be in coincidence with each other. The ordering of the transitions within a structure is made from intensity relationships and on consistency requirements of the excitation energies when more than one decay path is possible.

The $E_\gamma - E_\gamma$ coincidence matrix is analysed using the `escl8r` program from the Radware package [15]. This program enables the user to examine the coincidence relationships in the matrix by setting gates on individual transition energies. The two-dimensionality of the matrix allows a slice, set by the gate, to be taken from the matrix producing a one-dimensional spectrum as a result. The spectrum provides information on which detected γ rays have been in coincidence with the one that the gate was set on. It is this coincidence information that allows a level scheme to be built for a specific nucleus.

3.6 Angular Distributions

Depending of the multipolarity (L) of an emitted γ-ray its emission angle relative to the nuclear spin orientation will follow a characteristic probability distribution. Therefore, an angular distribution can provide information of the multipolarity of a given transition. However, conclusive angular distribution information can be difficult to obtain due to insufficient statistics, wrong assumptions of the nuclear spin alignment and/or mixing of different multipolarities. The angular distribution can be written [16]:

$$W(\theta) = a_0 + a_2 \cos^2\theta + a_4 \cos^4\theta + \ldots + a_{2L} \cos^{2L}\theta \tag{3.1}$$

where θ is the angle between the direction in which the γ-ray was emitted and the axis of the incoming beam. In heavy-ion reactions the angular momentum vectors (spin orientation) of the fusion-evaporation products are polarised and are distributed close to the plane perpendicular to the beam direction. The attenuation coefficients, a_n, of the spin alignment can be found in tables [17]. The radiation detected in the experiments described in this thesis have either magnetic dipole (M1) or electric quadrupole (E2) character. However, transitions may show a mixed multipolarity, e.g. in a M1 it is common with an E2 admixture. The angular distribution will then be something in between that of a M1 and that of an E2 transition.

Since the JUROGAM array has the detectors distributed in six rings relative to the beam direction, the ring dispersion permits the study of how the intensity of a particular transition is distributed over different angles relative to the beam direction. Comparing the experimental result with theoretical values deduced from equation 3.1 allows the identification of a certain multipolarity for a given transition. When the statistics are low, an approximate method can be used to obtain an angular distribution. The intensity, I_γ, of the transition of interest in the backward angle (158°) is compared with the intensity in the 90° direction. A ratio, R, is

formed of the two measured intensities according to:

$$R = N\left[\frac{I_\gamma(158^\circ)}{I_\gamma(86^\circ) + I_\gamma(94^\circ)}\right] \tag{3.2}$$

where N is a normalisation constant to account for the different number of detectors in each ring. The ratio is compared with the same ratio taken from previously assigned γ-ray transitions (pure E2's or M1's) in more strongly populated fusion-evaporation channels in the experiment. Typical values of R for these stretched quadrupole and stretched dipole transitions were 1.2 and 0.8, respectively.

Once the multipolarities of the γ-ray transitions are deduced, and knowing the band-head spin, each excited state in the level scheme can, in principle, be assigned a spin value. Based on other information, such as γ-ray branching ratios, internal conversion coefficients etc, some conclusions can also be drawn about the parity of a given state, even though the angular distributions contain no information on the electromagnetic character of a transition. For direct measurement of the electromagnetic character, linear polarisation information is needed. Such information is, however, not available for the JUROGAM detectors.

3.7 Measuring the Half-life

The decay time of any charged particle decay in the DSSD can be extracted using the absolute time information provided by the TDR system. Once a charged particle decay is detected in the DSSD its location and time are recorded. By applying an energy gate on the decay in question and correlating back in time, searching in the same pixel as the decay occurred for an earlier recoil event, the proton or alpha emitting nucleus can be identified as the mother of the decay. The time difference extracted from these events constitutes the decay time and is plotted in a decay spectrum showing the number of decays as a function of decay time.

It is not clear a priori what correlation time to use in order to search for a proton or alpha decay. It depends greatly of the background due to random correlations and the half-life in question. If the statistics are low and the half-life relatively short compared to the inverse of the count rate of an individual pixel, a longer correlation time can be used since every event may be valuable. Usually a correlation time of about three half-lives is often used, but if the decay is very fast compared to other channels four or five times the half-life can be used as correlation time. A histogram of the exponential α decay time distribution is shown in figure 3.5.

The standard way of extracting the mean lifetime τ of decay spectra with low statistics and low background is with the Maximum-Likelihood method [18]. The lifetime τ is obtained by summing all the time differences, $t_i = t_1, t_2, \ldots, t_n$, and divide by the number of detected decay events, n, as follows:

$$\tau = \frac{1}{n}\sum_{i=1}^{n} t_i \tag{3.3}$$

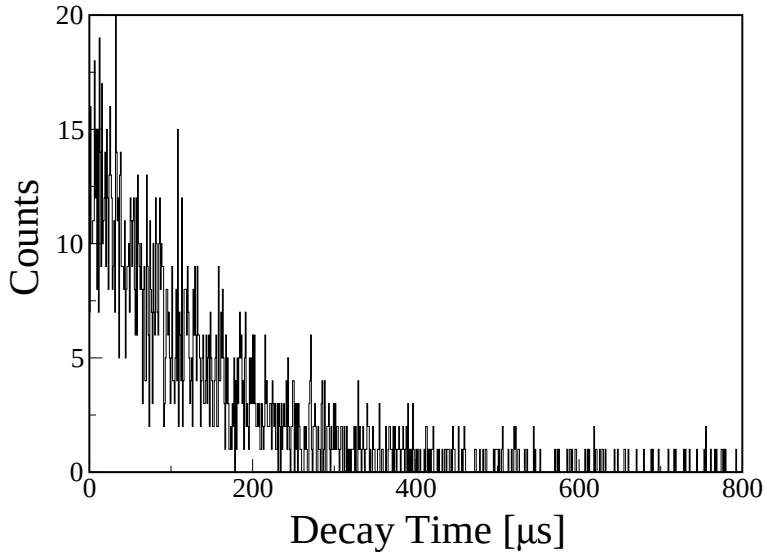

Figure 3.5: Time spectrum for the α decay of ^{110}Xe. The decay time spectrum is made with additional correlation of requiring a ^{106}Te daughter decay in the same pixel. The half life extracted from this spectrum using the Maximum-Likelihood method is calculated to be 93(3) μs.

If the half-life is not significantly shorter in comparison with the search-time T, a correction has to be made concerning that cut-off time. The corrected lifetime τ can then be obtained through:

$$\tau = \frac{1}{n}\sum_{i=1}^{n} t_i + \frac{T}{e^{T/\tau} - 1} \tag{3.4}$$

Equation 3.4 has to be solved iteratively. This is achieved numerically by forming the function $f(\tau) = 0$ from equation 3.4 and evaluate for τ until the function converges. The error bars for the measured half-lives are determined with equation 3.4. The procedure is described in [19] where the approximate upper (τ_u) and lower (τ_l) error limits are given as:

$$\tau_u \approx \frac{\tau}{1 - \frac{1}{\sqrt{n}}} \tag{3.5}$$

$$\tau_l \approx \frac{\tau}{1 + \frac{1}{\sqrt{n}}} \tag{3.6}$$

For large n (n>10), the approximate error is sufficiently close to the exact solution.

The half-life $t_{1/2}$ can then be computed as:

$$t_{1/2} = \tau ln2 \tag{3.7}$$

For a decay time spectrum with ample statistics an exponential fit is sufficient. The lifetime can be extracted by fitting a sum of two exponential functions to the data:

$$N = Ae^{-t/\tau} + Be^{-rt} \tag{3.8}$$

The lifetime τ is thus a parameter obtained from the fit. The parameter r is related to the background of random coincidence events and is given by the recoil rate per pixel of the DSSD. The half-life of ^{169}Ir was extracted using this method.

Chapter 4

Theoretical Framework

Theoretical nuclear structure models attempt to describe nuclear properties in the ground states as well as in various excitation modes. No single model can, as yet, describe all the observed nuclear properties within one framework. There are basically two phenomenological ways of describing the nucleus. "Microscopic" models deal with individual nucleons, where the interaction between them is approximated by a mean-field plus residual interaction (e.g pairing). Single particle energy levels in the nuclear shell model is an example of information predicted by such a model. Macroscopic models on the other hand, deal with collective phenomena, such as rotational and vibrational excitation modes of the nuclear medium. These approaches can be combined, using for example the microscopic-macroscopic shell correction method developed by Strutinsky [20].

This chapter will outline some models used to interpret the experimental data of this work. The new experimental information found in this work will also be compared with theoretical predictions.

4.1 Describing Nuclear Deformation

Nuclei can exhibit pronounced deformations, both in their ground states and in different excitation modes. The shape of a deformed nucleus is often described in theoretical models with an expansion in spherical harmonics. A set of deformation parameters is used to quantatively describe the shape of the nucleus. In a 'standard' Hill-Wheeler parametrisation [21] of the nucleus, two of them are denoted β_2 and γ. The parameter β_2 is used to describe the quadrupole deformation, in principle the elongation, of the nucleus. The nucleus is said to be *prolate* when two of the principal axes are of the same length while the third axis is longer. If the third axis is shorter than the two equal principal axes, the nucleus is said to have an *oblate* shape. The parametrisation is valid for $\beta_2 \geq 0$, and using only half the polar plane $\gamma = 0°$ and $\gamma = -120°$ gives prolate shapes, while $\gamma = 60°$ and $\gamma = -60°$ gives oblate shapes. For pure prolate and oblate shapes we have to distinguish

between *collective* and *non-collective* rotations. Collective rotation is described when the nucleus has the rotational axis *perpendicular* ($\gamma = 0°$ and $\gamma = -60°$) to the symmetry axis, and the nucleus is subjected to "non-collective" rotations ($\gamma = 60°$ and $\gamma = -120°$) when the rotation axis and symmetry axis coincide. The parametrisation of the nuclear shape is depicted in figure 4.1.

In many cases, e.g ^{169}Ir, the nucleus seem to depart from axial symmetry, needing an additional parameter in order to describe this degree of freedom. The γ parameter describes how *triaxial* the nucleus is, meaning that the nucleus can have all axes of different length. All intermediate γ values besides those mentioned above describe a triaxial nucleus.

4.2 The Rotating Frame

Rotation is a collective mode of excitation of a deformed nucleus found in different regions of the nuclear chart. Unlike a classical rotor, collective rotation around a symmetry axis is not quantum mechanically meaningful. This in turn implies that only a deformed nucleus can be said to be rotating. In order to interpret the experimental data and analyse rotational spectra, or level schemes, in view of the cranked shell model formalism, a transformation has to be performed into the rotating frame of the nucleus. Let I be the total angular momentum of the rotating nucleus, ω denote the rotational frequency and K the angular momentum projection onto the symmetry axis (3-axis) of a prolate nucleus (see figure 4.2). The component I_x of the angular momentum projected to the principle axis (1-axis), which represents the axis of rotation, can then be written:

$$I_x = \sqrt{\left(I + \frac{1}{2}\right)^2 - K^2} \tag{4.1}$$

The rotational frequency ω, expressed as $\hbar\omega$ in units of MeV, of the rotating nucleus can then be written:

$$\hbar\omega = \frac{dE}{dI_x} = \frac{E_i - E_f}{I_{xi} - I_{xf}} \tag{4.2}$$

where i denotes the initial level and f the final level for a γ-ray transition. For a stretched quadrupole transition (E2) in a rotational band, the rotational frequency can be approximated by:

$$\hbar\omega \approx \frac{E_\gamma}{2} \tag{4.3}$$

where E_γ denotes the γ-ray transition energy between two states.

In order to isolate the effect of the aligned angular momentum, $i(\omega)$, the angular momentum of a reference rotor is subtracted from I_x:

$$i(\omega) = I_x(\omega) - I_{ref}(\omega) \tag{4.4}$$

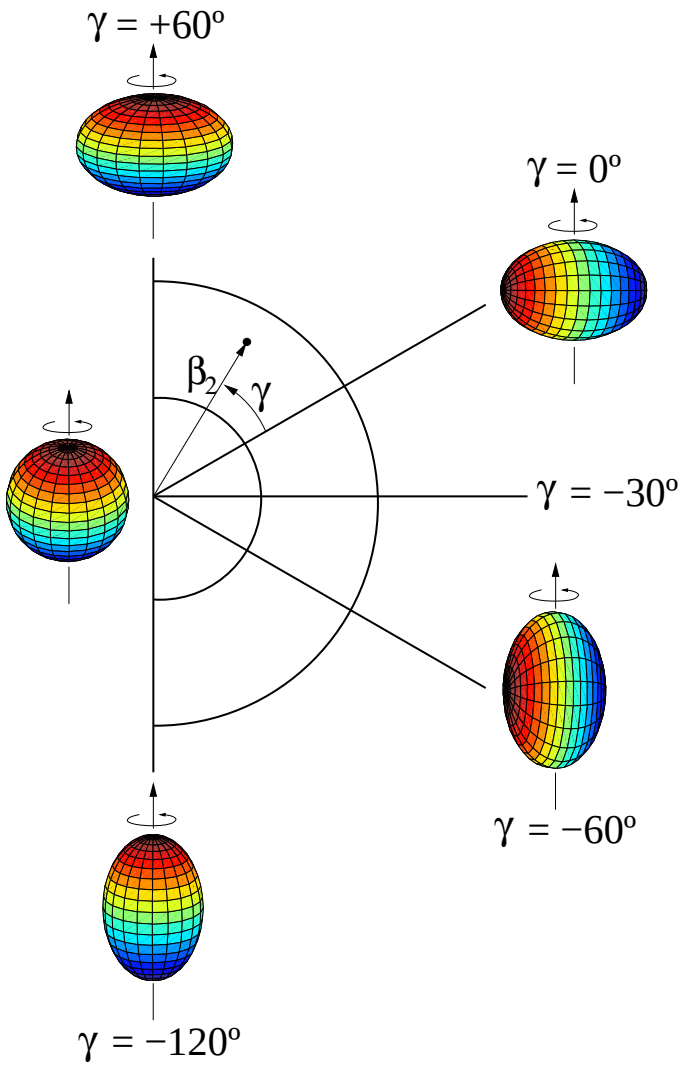

Figure 4.1: Schematic representation of the (β_2,γ)-parametrisation of the nuclear shape. The parameters corresponding to prolate and oblate shapes as well as collective and non-collective rotation are described in the text. The picture is adopted from [1].

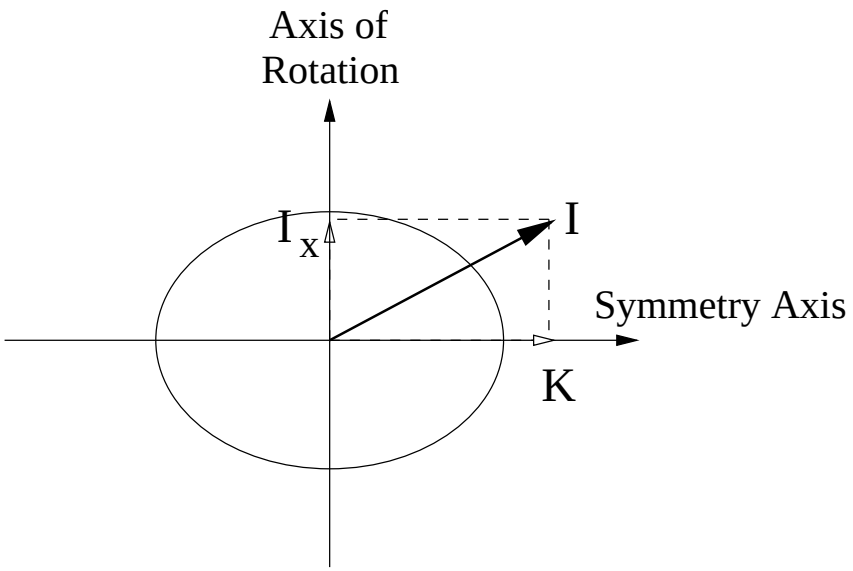

Figure 4.2: Projection of the total angular momentum I onto the symmetry axis and the rotational axis, which defines the K and I_x quantum numbers, respectively.

The reference angular momentum, I_{ref}, of the reference rotor is taken from the Harris expansion [22] as:

$$I_{ref}(\omega) = (\mathcal{J}_0 + \mathcal{J}_1\omega^2)\omega/\hbar \tag{4.5}$$

$\mathcal{J}_0$ and $\mathcal{J}_1$ are the so called Harris parameters, usually adjusted so that the "core" characteristic of the moment of inertia is reproduced. If an odd-N, odd-Z or odd-odd nucleus is studied, usually the parameters of the closest even-even core is taken. A plot of $i(\omega)$ as a function of rotational frequency is a way of showing single-particle effects, i.e. how the angular momentum vectors for valence nucleons are changing as a function of frequency, where a sudden change in $i(\omega)$ at some frequency can point to a breaking of a pair of nucleons. Although this method of presenting data (in a model dependent way) is very effective, care has to be taken when the nucleus is very deformation-soft. If the nucleus is sensitive to shape changes within a relatively small energy interval, and hence changing the moment of inertia of the nucleus, it can be difficult to know which Harris parameters to use.

The single-particle excitation energy can be obtained in the same manner as the aligned angular momentum, where the single particle excitation energy, e', in the rotating frame (Routhian) can be written:

$$e'(\omega) = E(\omega) - \omega I_x(\omega) - E_{ref}(\omega) \tag{4.6}$$

where the reference rotor energy is written [22]:

$$E_{ref}(\omega) = \frac{1}{8\mathcal{J}_0} - \frac{\omega^2}{2}\mathcal{J}_0 - \frac{\omega^4}{4}\mathcal{J}_1 \tag{4.7}$$

4.3 The Cranked Shell Model

The cranked shell model [23, 24] describes how the nucleons move in a potential well, e.g. a Woods-Saxon potential, that is *rotating* with angular frequency ω. The model then describes the collective rotation around one of the principle axes as a sum of single-particle angular momenta. The main differences compared to the shell model are that the nuclear potential is deformed and rotating.

Rotating the system is obtained by means of applying a rotation operator $\mathcal{R}(\omega t) = e^{-i\omega t\widehat{J}_x/\hbar}$ to the time independent Hamiltonian $\widehat{H}_0$. The *cranking* Hamiltonian $\widehat{H}^\omega$ can then be related to $\widehat{H}_0$ through:

$$\widehat{H}^\omega = \widehat{H}_0 - \omega\widehat{J}_x \tag{4.8}$$

where $\widehat{J}_x$ is the angular momentum operator along the rotation axis x, which is perpendicular to the symmetry axis of the nuclear shape. Applying the cranking Hamiltonian to a nuclear wave function produces the energy eigenvalues, which are called *Routhians*. These single-particle Routhians in the rotating frame, together with a Strutinsky shell correction term [20] and the liquid drop energy are the constituents to calculate the *total Routhian energy* E^ω_{tot}. The Total Routhian Surface (TRS) plots (described in section 4.4), which are produced with the E^ω_{tot}, form a vital part in interpreting the results in this work.

4.3.1 Signature

The total angular momentum I is not a conserved quantum number in the cranking model. However, the cranking Hamiltonian $\widehat{H}^\omega$ derived above is invariant with respect to rotation with an angle π around the rotational axis. The operator $\mathcal{R}$ for rotating the nucleus by an angle π around the the x-axis is given as:

$$\mathcal{R} = e^{-i\pi\widehat{J}_x} \tag{4.9}$$

and the eigenvalues of the operator are denoted $r = e^{-i\pi\alpha}$. Both r and (preferentially) α are called the *signature* quantum number which is a conserved quantity. The relation between spin and signature is given by:

$$I = \alpha \ (mod\ 2) \tag{4.10}$$

Another symmetry in the cranking model is that of space inversion $\mathcal{P}$, and hence also the parity π is a conserved quantum number. The parity can either be positive or negative. For a nucleus with an even number of nucleons the signature α can

take on values 0 or 1 and for an odd-A nucleus the signature can be $\pm\frac{1}{2}$. Thus, a rotational band in an odd-A nucleus with a sequence of levels differing by spin 1 is divided into two branches, each consisting of levels differing by spin 2 and classified by the signature quantum number $\alpha = \pm\frac{1}{2}$, respectively. The transitions within a band will be of E2 type, and those between bands will be of M1 or mixed M1/E2 type, since all states of the band have the same parity, i.e. the selection rules must be obeyed. The two branches are said to be *signature partners* of a rotational band. Experimentally, one often observes an energy staggering in the rotational bands and this may be refered to as *signature splitting* [25]. The favoured band is the branch that is pushed down in energy, while the unfavoured band is the one being pushed up in energy. An example of this can be found in ^{169}Ir for Band 1.

When a nucleus is departing from being axially symmetric, i.e. adopts a triaxial shape, the angular momentum projection (K) onto the symmetry axis is no longer a good quantum number. The nuclear wave function will no longer contain a pure K-component. The triaxial deformation will mix-in lower K-value components, such as K=1/2, into the wave function thereby creating a signature splitting between the two signature partners of the band by means of an effect similar to the classical Coriolis effect. The energies of the states in a rotational band for an odd-A nucleus can be expressed [26]:

$$E_{IK} = E_K + \frac{\hbar^2}{2\mathcal{J}}\left[I(I+1) - K^2 + \delta_{K\frac{1}{2}}a(-1)^{I+\frac{1}{2}}\left(I+\frac{1}{2}\right)\right] \tag{4.11}$$

where the second term within the brackets is responsible for the energy splitting of the signatures. For different spins (I) a state will be either pushed up or down in energy depending on the sign of the $(-1)^{I+\frac{1}{2}}$ factor. Although the mechanism behind triaxiality is poorly known it is generally believed that the observed signature splitting can be an experimental sign of a triaxially deformed nucleus.

4.4 Total Routhian Surfaces

The Total Routhian Surface (TRS) [27, 28] plot is a useful tool for a theoretical interpretation of the experimental results obtained in this work. The TRSs are sensitive to a specific nucleonic configuration and show the energy in the rotating system as a function of the deformation parameters β_2 and γ. A minimum of such a plot shows the favoured deformation for the nucleus at a specific rotational frequency and particle configuration [29, 30]. The total Routhian energy is calculated for a set of deformation parameters β_2 and γ, first chosen as equally spaced points in a two-dimensional x-y-grid (see figure 4.3). The parametrisation of the grid being for $x = \beta_2\cos(\gamma + 30^\circ)$ and for $y = \beta_2\sin(\gamma + 30^\circ)$. The calculated energy values are then plotted with contour lines for equally spaced energies.

An example from of a TRS plot from the this work is presented in figure 4.3. It shows the favoured deformation for ^{110}Xe (panel **a)**) and, for comparison, the energy minimum for the nearest even-even isotopes $^{112-116}$Xe (panels **b)-d)**) at

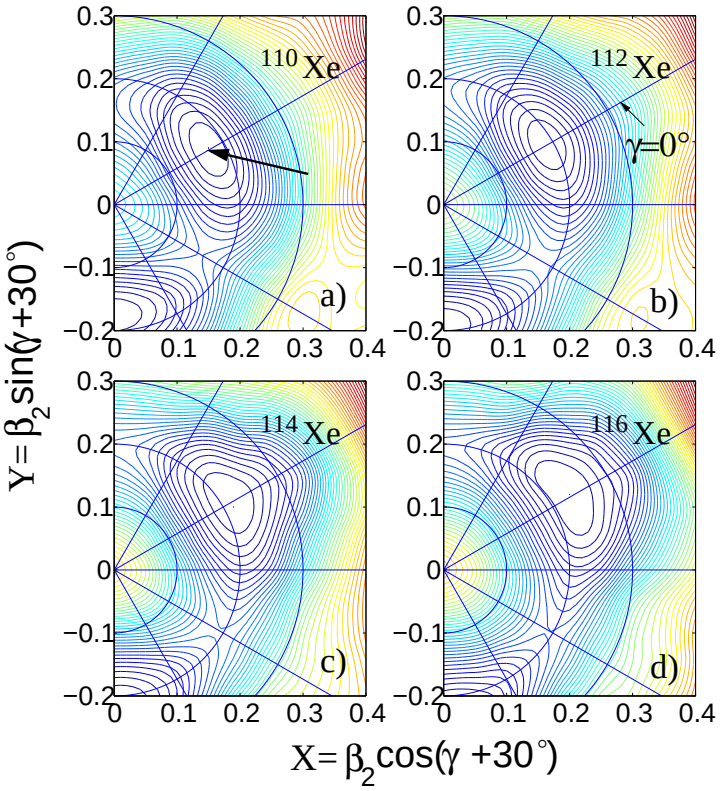

Figure 4.3: TRS plots at zero rotational frequency for the $(\pi, \alpha) = (+, 0)$ configuration of the even-even $^{110-116}$Xe isotopes. The arrow in panel **a)** points to the favoured (stable) energy minimum of the TRS, corresponding to an elongation of $\beta_2 = 0.17$ with $\gamma \approx 0$ (the line $\gamma = 0°$ is indicated in panel **b)**). The energy difference between contour lines is 100 keV.

zero rotational frequency. The only good quantum numbers for the wave functions in the rotating frame are the parity, π, and the signature, α. Therefore, each TRS is defined by the pair (π, α) and the rotational frequency, ω. The configuration in this case is (+,0) for all depicted xenon isotopes. From the plots in figure 4.3 it can be seen that all light Xe-isotopes are "soft" with respect to both deformation parameters β_2 and γ. This means that the nucleus may be susceptible to shape changes within a relatively small energy range. Panel **a)** shows for ^{110}Xe a small prolate β_2 deformation of 0.17 with the axial symmetry intact. The γ deformation is zero, hence indicating the two principal axes being of same length, but differing from the symmetry axis. From figure 4.3 it can also be inferred for the xenon isotopes, a larger β_2 deformation, and a more pronounced β_2 softness with increasing neutron number.

4.5 B(M1)/B(E2) values

The probability for a γ-ray transition from a specific collective rotational state is given by the B(M1) and B(E2) values for a magnetic dipole (M1) and an electric quadrupole (E2) transition, respectively. The ratio B(M1)/B(E2) between two such transition probabilities from a state with spin I to states with spin I-1 and I-2, respectively, can give valuable information of the configuration of the states connected by the transitions. The experimental ratios are obtained with the γ-ray transition energies and the intensities of the M1 and E2 transitions from the same state through the relation [31]:

$$\frac{B(M1; I \rightarrow I-1)}{B(E2; I \rightarrow I-2)} = 0.697 \frac{[E_\gamma(I \rightarrow I-2)]^5}{[E_\gamma(I \rightarrow I-1)]^3} \frac{1}{\lambda} \frac{1}{1+\delta^2} \quad \left[\frac{\mu_N^2}{e^2 b^2}\right], \tag{4.12}$$

where λ is the experimental branching ratio between an E2 and a M1 transition. It is taken as the ratio of the measured γ-ray intensities, T_γ, of the two transitions as

$$\lambda = \frac{T_\gamma(E2)}{T_\gamma(M1)} \tag{4.13}$$

The δ parameter is the amount of E2 admixture in the M1 transition. The experimentally deduced B(M1)/B(E2) ratios are compared to those obtained through the semi-classical formalism of Dönau and Frauendorf [32, 33]. Since the ratios are sensitive to the single particle configuration as well as to the nuclear quadrupole deformation, a comparison with the experimental B(M1)/B(E2) values will give information of the configuration and the deformation.

The B(E2) transition probabilities are a measure of the nuclear collectivity. Therefore a plot of B(E2) values as a function of neutron number permits trends to be visualised of increasing/decreasing nuclear collectivity over an isotopic chain.

Normally B(E2) values are deduced from the level lifetimes, but lacking such information the experimental transition strength can be estimated from the empirical relationship between the 2_1^+ energies and the corresponding transition probability [34] as:

$$B(E2; 2_1^+ \rightarrow 0_1^+) \approx 0.66 E(2_1^+)^{-1} Z^2 A^{-0.69} \quad [e^2b^2] \tag{4.14}$$

This relationship is used to interpret the trend of the B(E2) values in the lightest xenon isotopes and compare them with theoretical model calculations presented in [35]. The models used to calculate the B(E2) values are based on the quadrupole deformation obtained through TRS calculations, hence the B(E2) values are *model dependent* from a collective rotational point of view. So in a transitional region from a rotational collective to a single particle regime, the theoretically calculated B(E2) values may not reflect the real strengths. The comparison is more relevant for *trends* rather than for a quantitative assessment of the B(E2) values.

Chapter 5

Summary of Papers

The experimental results and the author's contribution to **papers I** and **II** are briefly discussed in the following.

This work describes experiments to produce and study the extremely neutron deficient ^{169}Ir and ^{110}Xe atomic nuclei. They are situated in quite different mass regions of the nuclear chart and have different characteristics. The common theme, however, is the large excess of protons compared to stable isotopes making both nuclei unstable to α particle emission in their ground states (in ^{169}Ir there is an isomeric α decaying state as well). This α emission plus a short half life make both nuclei suitable to be studied with the RDT technique. There are currently no other techniques available to access the structure of such weak fusion-evaporation channels.

Both experiments were performed at the Accelerator Laboratory of the University of Jyväskylä, Finland. The experimental techniques to produce and study these nuclei were similar. Fusion evaporation reactions were used to produce them and the gas-filled RITU separator coupled to the GREAT spectrometer was used to detect them. Prompt γ rays at the target position were detected with the JUROGAM Ge-detector array. Both nuclei were identified using the RDT technique. The aim of the experiment involving ^{169}Ir was primarily to study shape evolution and band crossings in ^{170}Pt (see ref. [36]). One of the prominent 'side' channels in the fusion evaporation experiment was ^{169}Ir for which excited states were previously unknown. Although the author was not personally involved in the experiment, full responsibility was taken for the subsequent off-line analysis of the data. The experiment targeting ^{110}Xe had the aim of probing the N≈Z ^{100}Sn region, offering a chance to search for enhanced T=1 isoscalar n-p pairing, and the possibility of investigating the collective features of the light Xe-isotopes as the N=Z line is approached. Energy systematics of 2_1^+ and 4_1^+ states and empirical transition probabilities of the derived states were compared with theoretical predictions.

5.1 Paper I

The ^{60}Ni+^{112}Sn→^{169}Ir*+p2n fusion evaporation reaction was used to populate excited states in ^{169}Ir. The ^{60}Ni ions impinging on the 800 μg/cm^2 thin ^{112}Sn taget were accelerated to 266 MeV by the K130 cyclotron. The cross section for the reaction was measured to $\sigma \approx$120 μb. Excited states for the odd-A ^{169}Ir isotope were established for the first time and a level scheme was proposed. Also, two α decaying states were identified and confirmed from earlier work. The more strongly populated α decaying state in the experiment is a low-lying isomeric state, 153(24) keV above the ground state. The γ-ray transitions identified were from excited states built on this isomeric state, which was assigned to be based on a $h_{11/2}$ configuration. The ground state was assigned as the $s_{1/2}$ configuration.

The $h_{11/2}$ state was predicted by TRS calculations to posses a small prolate deformation of β_2=0.14 at a triaxial shape with γ=-16°. The configuration assignment of the yrast $h_{11/2}$ band-head and the deformation parameters were in agreement with the deduced B(M1)/B(E2) ratios. The γ-ray cascade feeding the isomeric α decaying state exhibits a rotational structure consistent with a $h_{11/2}$ proton coupled to a triaxially deformed core.

The coupled band structure in ^{169}Ir shows a large signature splitting between the two branches in the band. This continues the trend of increasing signature splitting with decreasing neutron number for the lightest Ir-isotopes. Interestingly the theoretical prediction from TRS calculations point to the *oppostite* trend of a slight *decrease* of triaxiality with decreasing neutron number for the odd-A $^{169-175}$Ir isotopes. This is thus contrary to the standard interpretation of increasing γ deformation with increasing signature splitting, and may imply an inability of the model to predict the shape evolution of the lightest Ir isotopes (TRS calculations are known to have good predictive power of nuclear shapes close to stability). On the other hand the γ-softness of the calculated energy minima tends to increase with increasing neutron number. Taking this into account, the effective γ deformation may be different from that in a given minimum point in a TRS plot. Further investigation is needed.

The author performed the data analysis and was the principal author of the paper.

5.2 Paper II

The extremely neutron-deficient N=Z+2 ^{110}Xe isotope was produced using the ^{54}Fe+^{58}Ni→^{110}Xe*+2n reaction at a beam energy of 195 MeV. Gamma-ray transitions were identified for the first time. The production cross section was extremely low, $\sigma \approx$50 nb, close to the limit of what is possible for in-beam measurements with state-of-the-art equipment for nuclear spectroscopy. The identification of ^{110}Xe was made with the aid of its daughter, ^{106}Te, α decay. Despite the weak population

rate is was possible, thanks to the selectivity of the RDT technique, to identify the three lowest excited states in ^{110}Xe.

The energy level of the first excited 2_1^+ state was compared with the systematic trend from heavier even-even Xe-isotopes. The new striking results for $^{110}_{54}Xe_{56}$ show that the excitation energy of the lowest excited 2_1^+ state differs only by 4 keV (less than 1 %) from that of ^{112}Xe while the excitation energy of the 4_1^+ state in ^{110}Xe is *lower* than that of its ^{112}Xe counterpart. This is contrary to the expected trend of increasing 2_1^+ and 4_1^+ energies as the closed N=50 shell is approached.

The empirically reduced transition probability, B(E2), for the 2_1^+ state, revealed a slight *increase* for ^{110}Xe as compared with heavier even-even isotopes. This trend is also in disagreement with theoretical predictions. The experimental results thus point to an *increase* in collectivity, while the theoretical models predict a *decrease* in collectivity as the N=Z line is approached, coinciding with the expected double shell closure at ^{100}Sn. It is proposed that the experimental findings suggesting an increase in collectivity is possibly a result of a strong dynamical neutron-proton pairing. This residual interaction between unlike nucleons may be especially pronounced where the valence particles occupy identical orbitals, making for an increased spacial overlap between the neutron and proton wave functions. The experimental results from this paper make it necessary for nuclear models to incorporate the proposed residual n-p pairing interaction in order to explain the behaviour of ^{110}Xe.

The author was responsible for the experiment, performed the data analysis and wrote part of the paper.

Acknowledgements

Although writing a licentiate thesis is a lone effort, the experimental results which the thesis is based upon are obtained with the help from many collaborators. Foremost I like to thank my supervisor Bo Cederwall for his ever continuing enthusiasm and support. His guidance and optimistic appraisal of my work are a constant source of gratitude. I'm particularly thankful for the opportunity to spend my first year at the JYFL Accelerator Laboratory at the University of Jyväskylä in Finland, and for the hands-on experience I attached to myself in this gem of a lab. I thank Rauno Julin for his inspiring guidance, and for showing me the intricacies of cross-country skiing. My gratitude also extends to Cath Scholey, Iain Moore, Panu Rahkila and Paul Greenlees for making my year one of the most memorable in my life.

On home turf I like to honour my office mates Karin Andgren, Baharak Hadinia and Anton Khaplanov for the good nature and pleasant atmosphere they create in my working surroundings, and the invaluable help they give me concerning the multitude of computer troubles that arise. In the same vein I would also like to thank Torbjörn Bäck for providing computer support way beyond his duties, and for the many interesting conversations on every topic conceivable. I would also like to thank all my colleagues at KTH whom I have the pleasure to exchange words with from time to time. I especially enjoy the company of Daniel Karlgren and Ela Ganioğlu and the good humour they spread around their appearance. I'm also very thankful for all the senior staff members, Arne Johnson for proof-reading my articles and thesis, Lars-Olov Norlin, Ramon Wyss and Roberto Liotta for discussions on various physic topics.

Finally I would like to extend a special thank to whoever invented/discovered the fermentation process of grape juice. The end result of this miraculous process plays a vital role for the sanity and well being of the author, and for the successful completion of this thesis.

Bibliography

[1] T. Bäck, *Spectroscopy of Neutron Deficient Nuclei in the $A \approx 90$ and $A \approx 170$ Mass Regions*, (2002).

[2] C.W. Beausang *et al.*, Nucl. Instr. Meth. A313, 37 (1992).

[3] C.R. Alvarez *et al.*, Nucl. Phys. News 3, 3 (1993).

[4] M. Leino *et al.*, Nucl. Instr. Meth. B99, 653 (1995).

[5] M. Leino, Nucl. Instr. Meth. B126, 320 (1997).

[6] A. Ghiorso *et al.*, NIM A269, 192 (1988).

[7] N. Bohr, Phys. Rev. 59, 270 (1941).

[8] R.D. Page *et al.*, Nucl. Instr. Meth. Phys. Res. B204, 634 (2003).

[9] http://www.jyu.fi/physics

[10] I.H. Lazarus *et al.*, IEEE Trans. Nucl. Sci. 48, 567 (2001).

[11] G.F. Knoll, in *Radiation Detection and Measurement*, (John Wiley & Sons, 2^{nd} Edition 1989), p.121.

[12] R.S. Simon *et al.*, Z. Phys. A325, 197 (1986).

[13] E.S. Paul *et al.*, Phys. Rev. C51, 78 (1995).

[14] P. Rahkila, Slide report of Midwinter workshop on tagging methods and experiments, Jyväskylä, (2004).

[15] D.C. Radford *et al.*, Nucl. Instrum. Meth. A361, 297 (1995).

[16] K.S. Krane *et al*, Nucl. Data Tables 11, 351 (1973).

[17] T. Yamazaki, Nucl. Data, 3(1) (1967).

[18] E. Segrè, *Nuclei and Particles, An Introduction to Nuclear and Subnuclear Physics*. W.A. Benjamin, New York, 1964.

[19] K.H. Schmidt *et al.*, Z. Phys. A, 316:19 (1984).

[20] V.M. Strutinsky Nucl. Phys. A95, 420 (1967).

[21] D.L. Hill and J.A. Wheeler, Phys. Rev. 89, 1102 (1953).

[22] S.M. Harris, Phys. Rev. B138, 509 (1965).

[23] D.R. Inglis, Phys. Rev. 96, 1059 (1954).

[24] D.R. Inglis, Phys. Rev. 103, 1786 (1956).

[25] K. Hara and Y. Sun, Nucl. Phys. A537, 77 (1992).

[26] S.G. Nilsson and I. Ragnarsson, in *Shapes and Shells in Nuclear Structure*, (Cambridge University Press, 1995) p.189.

[27] W. Nazarewicz, R. Wyss and A. Johnson, Nucl. Phys. A503, 285 (1989).

[28] W. Satuła and R. Wyss, *Phys. Scripta*, T 56, 159 (1995).

[29] R. Wyss *et al.*, Phys. Lett. B215, 211 (1988).

[30] R. Wyss *et al.*, Nucl. Phys. A503, 244-262 (1989).

[31] S. Juutinen *et al.*, Nucl. Phys. A526, 346-364 (1991).

[32] D. Dönau and S. Frauendorf, in *Proceedings of the Conference on High Angular Momentum Properties of Nuclei, Oak Ridge*, edited by N. R. Johnson (Harwood, New York, 1983) p. 143.

[33] F. Dönau *et al.*, Nucl. Phys. A471, 469 (1987).

[34] S. Raman *et al.*, At. Data Nucl. Data Tables 42 1 (1989).

[35] S. Raman, J.A. Sheikh, K.H. Bhatt, Phys. Rev. C52, 1380 (1995).

[36] D.T Joss *et al.*, Phys. Rev. C74, 014302 (2006).